RSC Advances

ROYAL SOCIETY OF CHEMISTRY

PAPER

View Article Online
View Journal | View Issue

Check for updates

Cite this: *RSC Adv.*, 2023, **13**, 34262

Received 22nd September 2023
Accepted 16th November 2023

DOI: 10.1039/d3ra06467k

rsc.li/rsc-advances

A DFT study towards dynamic structures of iron and iron carbide and their effects on the activity of the Fischer–Tropsch process†

Qiang Yin,[ac] Hanqing Wang,*[bc] Jinping Zhao,[b] Chengjun Li[b] and Yu Mao *[d]

The Fe-based Fischer–Tropsch synthesis (FTS) catalyst shows a rich phase chemistry under pre-treatment and FTS conditions. The exact structural composition of the active site, whether iron or iron carbide (FeC_x), is still controversial. Aiming to obtain an insight into the active sites and their role in affecting FTS activity, the swarm intelligence algorithm is implemented to search for the most stable Fe(100), Fe(110), Fe(210) surfaces with different carbon ratios. Then, *ab initio* atomistic thermodynamics and Wulffman construction were employed to evaluate the stability of these surfaces at different chemical potentials of carbon. Their FTS reactivity and selectivity were later assessed by semi-quantitative micro-kinetic equations. The results show that stability, reactivity, and selectivity of the iron are all affected by the carbonization process when the carbon ratio increases. Formation of the carbide, a rather natural process under experimental conditions, would moderately increase the turnover frequency (TOF), but both iron and iron carbide are active to the reaction.

Introduction

As one of the most important catalytic processes in industry, Fischer–Tropsch synthesis (FTS) converts synthesis gas (CO + H_2) into a wide spectrum of long-chain hydrocarbons and oxygenates.[1] Four transition metals, namely Fe, Co, Ni, and Ru, have been used in catalyzing the FTS; however, only Fe and Co are industrially feasible because the methane selectivity on Ni is undesirably high, and the resources of Ru are rather limited.[2] Both Fe and Co are suitable for low-temperature FTS (473–513 K) while only Fe is used at high temperature (573–623 K).[3] In recent years, Fe-based FTS catalysts have attracted increasing attention from researchers owing to their lower price, higher resistance to contaminants, and higher activity of the water–gas shift (WGS) reaction.[4,5]

The Fe-based FTS catalyst shows a rich phase chemistry under pretreatment and FTS conditions.[6] Industrially, small iron oxide crystallites (*e.g.* hematite, α-Fe_2O_3) are firstly reduced to magnetite (Fe_3O_4) irrespective with H_2, CO, or their mixture during the pre-treatment, and the catalyst then converts to a mixture of carbides, oxides, and metallic iron depending on the pre-treatment conditions.[2,7–11] Among the mixture, iron oxides, especially Fe_3O_4, are reported to be active for WGS reaction, while metallic iron and iron carbides are known for its ability to dissociate C–O bond at room temperature, thus reported to be active for FTS.[2,12,13] Experimentally, it is found that FTS activity increases with the extent of Fe_3O_4 conversion into iron carbides;[14–16] therefore, many researchers argue that the carbide is the active phase and responsible for high FTS activity.[4,10,17–19] Among them, Hägg iron carbide (χ-Fe_5C_2) is the most common one and has been investigated extensively.[7,10,11,15,20–23] In addition, other carbides surfaces, with the atomic ratio of C to Fe ranged from 0.33 to 0.50 (Fe_2C, $Fe_{2.2}C$, Fe_3C, Fe_7C_3, *etc.*), have also been studied.[14,24–27]

However, most of these studies[28–30] are based on comparing energy barriers of elementary steps on some facets of pure Fe and Fe carbide, without investigating their relative stability and overall micro-kinetics. In addition, the exact mechanism to produce hydrocarbons over iron carbide phases is largely unknown. Therefore, the exact structural composition of the active phase and the role of these phases are still controversial due to the limitations of *in situ* characterization of the catalyst.[2,14] Claims of catalytic activity of Fe_3O_4,[31–33] pure Fe,[16,34,35] and iron carbides[26,36,37] in FTS are all found in previous studies. From the Mössbauer emission spectroscopy (MES), Niemantsverdriet *et al.*[34] found that the carbides can only be observed in coexistence with pure Fe or just after it disappeared. Therefore, the carbide during FTS may be a poorly defined intermediate between pure Fe and known carbide structures.

---

[a] *Department of Forestry Engineering, School of Materials Science and Engineering, Central South University of Forestry & Technology, Changsha, China*

[b] *School of Civil Engineering, Central South University of Forestry & Technology, Changsha, China. E-mail: hqwang@csuft.edu.cn*

[c] *Hunan Engineering Research Centre of Full Life-cycle Energy-efficient Buildings and Environmental Health, Central South University of Forestry and Technology, Changsha, Hunan, China*

[d] *School of Chemical Sciences, University of Auckland, Auckland 1010, New Zealand. E-mail: yu.mao@auckland.ac.nz*

† Electronic supplementary information (ESI) available. See DOI: https://doi.org/10.1039/d3ra06467k

The working catalyst is likely to be a mixture of amorphous regions, in which the surface composition may differ from the bulk.[2,11,38]

In addition to rich phase chemistry, FTS is also regarded as one of the most complicated catalytic system owing to two facts: (i) there are scores of – if not hundreds of – elementary reactions interconnected with each other in FTS mechanism; (ii) both reactivity and selectivity should be considered since the reaction is aiming for long-chain hydrocarbon, rather than by-product methane. Generally, there are three types of mechanisms proposed in the literature:[3,39] the carbene mechanism,[40] the hydroxyl-carbene mechanism,[41] and the CO-insertion mechanism.[42] Supported by plenty of theoretical and experimental evidences,[43–45] the carbene mechanism is the most popular among them.[1,46–49] In this mechanism, CO adsorbs dissociatively into C and O on the surface, C then sequentially hydrogenated to give C_1 (CH_x, $x = 1$–3) species, and O gets removed from the surface as water. After that, the C_1 species can either be further hydrogenated to form methane, or couple with another C_1, resulting in C_2 species (CH_x–CH_y, x, $y = 0$–3). Similar hydrogenation and coupling processes continue to give long-chain hydrocarbons.[50–52]

In such a complicated catalytic reaction system, a lack of deep understanding of the active phase composition and corresponding reaction pathways greatly limits the design of better Fe-based FTS catalysts. Several questions remain to be addressed: (i) what is the influence of the reactions conditions on the dynamic structure of iron surfaces; (ii) what is the origin of the high activity, as claimed in many literature, of iron carbides;[50,53] (iii) what is the actual composition of the active phase during FTS. In this study, swarm intelligence algorithm[54] was implemented to search Fe(100), Fe(110), Fe(210) surfaces with different carbon ratios, which extends well beyond the current literature that focus on investigating a specific type of iron or carbide phase. It is perhaps more close to the realistic FTS system since the catalyst activity is determined by the nature of the surface phase rather than the bulk phase composition.[38] Then, the stability of these surfaces was evaluated by *ab initio* atomistic thermodynamics and Wulffman construction[55–57] at different reaction conditions. Their FTS reactivity and selectivity were later semi-quantitively assessed by a micro-kinetic model developed by Chen *et al.*[46,58–60] and a general discussion was addressed on these results.

Methods

All calculations in the paper were carried out with the Perdew–Burke–Ernzerhof[61] functional using Vienna *ab initio* simulation package (VASP).[62,63] The project-augmented wave (PAW) method was used to represent the core–valence interaction.[64,65] For the calculations of total energy, a cut-off energy of 450 eV was set for plane wave basis sets to expand the valence electronic states. Spin polarization was included for all calculations to obtain an accurate description of magnetic systems. The values of magnetic moments of each layer by our calculation agree well with previous results.[66] For example, the magnetic moments of first and second layer atoms of Fe(110) are 2.61 and 2.36 μ_B, respectively, very close to 2.59 and 2.35 μ_B in the work of Kresse *et al.*[67] The agreement verifies the rationality of our computational setting. Also, the PBE functional have been extensively used in similar studies.[68–70] We have also tested the CO adsorption energy using different functionals, namely PBEsol and RPBE, and shows similar trends as that of PBE functional.

To obtain the free energy of species, some standard formulas of statistical mechanics were used to calculate the zero point energy (ZPE), thermal energy, and entropy derived from partition functions[71,72] (see Section SI-1 in the ESI† for detailed equations). The Brillouin zone was sampled with a *k*-point mesh of 4 × 4 × 1 for Fe(100), 4 × 3 × 1 for Fe(110), and 3 × 4 × 1 Fe(210) (see Section SI-2 in the ESI† for the illustrations of surface models and their cell parameters). Upper half of substrate layers and adsorbates were fully relaxed until the forces were lower than 0.05 eV Å^{-1} while the lower half of substrate layers were fixed. The adsorption energy of X is defined as:

$$E_{\text{ad}}^{\text{X}} = E_{(\text{X/substrate})} - E_{(\text{substrate})} - E_{(\text{X})} \tag{1}$$

where $E_{(\text{X/substrate})}$, $E_{(\text{substrate})}$, and $E_{(\text{X})}$ are the free energies of X adsorbed on the substrate, the substrate, and X in the gas phase, respectively. The more negative of E_{ad}^{I} is, the more strongly the species binds with the substrate. The transition states (TS) are determined by a constrained optimization scheme,[73,74] which are verified until (i) all forces on atoms vanish; and (ii) the total energy reaches maximum along the reaction coordination but minimum with respect to the rest of the degrees of freedom.

The most stable structures of Fe(100), Fe(110), and Fe(210) with different ratio of surface carbon are obtained using the swarm intelligence algorithm implemented in CALYPSO,[75,76] which is an effective tool to search for the global minimum of structures for many different systems[77–80] In CALYPSO, swarm intelligence, specifically the particle swarm optimization (PSO) algorithm, is employed to predict the crystal structures of materials based on their chemical compositions. The PSO algorithm is best-known for its ability to conquer large barriers of energy landscapes by making use of the swarm intelligence and by self-improving structures. This this study, it is used to search the potential energy landscape of the surface.[81]

For these surface models, 20 generations with 16 individuals in each generation are optimized during the structure evolution. Lower two layers are fixed as Fe bulk while top two layer are generated by CALYPSO by specifying the number of Fe and C atoms. All other parameters are default values of CALYPSO surface evolution. Furthermore, *ab initio* thermodynamics[82–84] was employed to evaluate the surface energy γ of iron carbide surfaces at experimental conditions:[7,14]

$$\gamma(T, P) = [G_{\text{sur}}(T, P, N_{\text{Fe}}, N_{\text{C}}) - N_{\text{Fe}}\mu_{\text{Fe}}(T, P) - N_{\text{C}}\mu_{\text{C}}(T, P)]/2\text{A} \tag{2}$$

where N_{Fe} and N_{C} are the number of Fe and C atoms; μ_{Fe} and μ_{C} represent their chemical potential, respectively. G_{sur} stands for the free energy of the surfaces and A is the area of the surface in the unit cell. In this study, bulk bcc Fe was used for reference energy of atomic Fe, and G_{sur} was calculate directly from DFT total energy since the vibrational contribution to the surface free energy is neglectable (less than 3% at 500 K).[7,20] It should be noted that the *ab initio* thermodynamics evaluate the stability at equilibrium state, which do not take the kinetic factor into account.

The crystal morphology of iron carbide is obtained from Wulffman construction,[55–57] which is the standard method for determining the equilibrium shape of bulk crystals by minimizing its orientation-dependent surface free energy for a given enclosed volume.[85,86] It offers a simple and rigorous way to describe the shape of nanoparticles by the surface energies of some (*hkl*) faces and the point group of the material.[87]

Results and discussion

Carbide surfaces obtained from CALYPSO

Fig. 1 illustrate the structures and relative energies of Fe(110) surface with different carbon ratio from 1 to 5 (results of Fe(100) and Fe(210) can be found in Section SI-3 in the ESI†). As shown in Fig. 1a and b a four-layer model was built for pure Fe(110) surface. In CALYPSO, the bottom two layers are fixed while the 2$^{\mathrm{nd}}$ layer is allowed to relax. The first layer is generated randomly by swarm intelligence algorithm along with a certain number of C atoms (one to five). After optimization, the most stable structures and their relative energies are displayed in Fig. 2 and 1c, respectively. This simulation method aligns closely with experimental observations. After pre-treatment, iron carbides form on the exterior of Fe_3O_4 or Fe crystallites, resulting in an enveloping core structure.[10,88]

In Fig. 2, the C atom tends to stay above the surface; for Fe(110)-1C, the energy of the structure with a surface C atom is ∼0.4 eV lower than that of the structure with a subsurface C. However, when there are more than three C atoms, two or three of them will diffuse to sub-surfaces due to the large repulsion between surface atoms. For Fe(110)-3C, the energy of the structure with all surface C is ∼0.08 eV lower than the second stable one; while the energy of the Fe(110)-4C with four surface C, on the other hand, is ∼0.1 eV higher than the most stable one. Similar conclusions can be made for Fe(100) and Fe(210) surfaces. In Fig. S1 and S2,† C atoms diffuse into sub-surfaces in 4C and 5C structures for both Fe(100) and Fe(210). It should be noted that for Fe(210)-5C, the most stable structure is the carbon deposit, which is reasonable since the deposit is easier to grow on the step facets.[72] It is well recognized that the C deposits (*e.g.* coke, graphitic carbon, and amorphous carbon) on the surface will lead to the deactivation;[2,34,37,89] therefore, in this study, any structure with two or more C atoms link together on the surface is regarded inactive, and the second most stable one of Fe(210)-5C is adopted for further activity analysis. It should be noted that those linking C atoms may be an artifact of the small size of the system. The more detailed examination of coke formation and its stability as the carbon ratio increases (*e.g.* employing large slab size for global optimization) is our future research endeavors.

Generally, iron surfaces show a variety of structures under different carbon concentration. Starting from the upper surface,

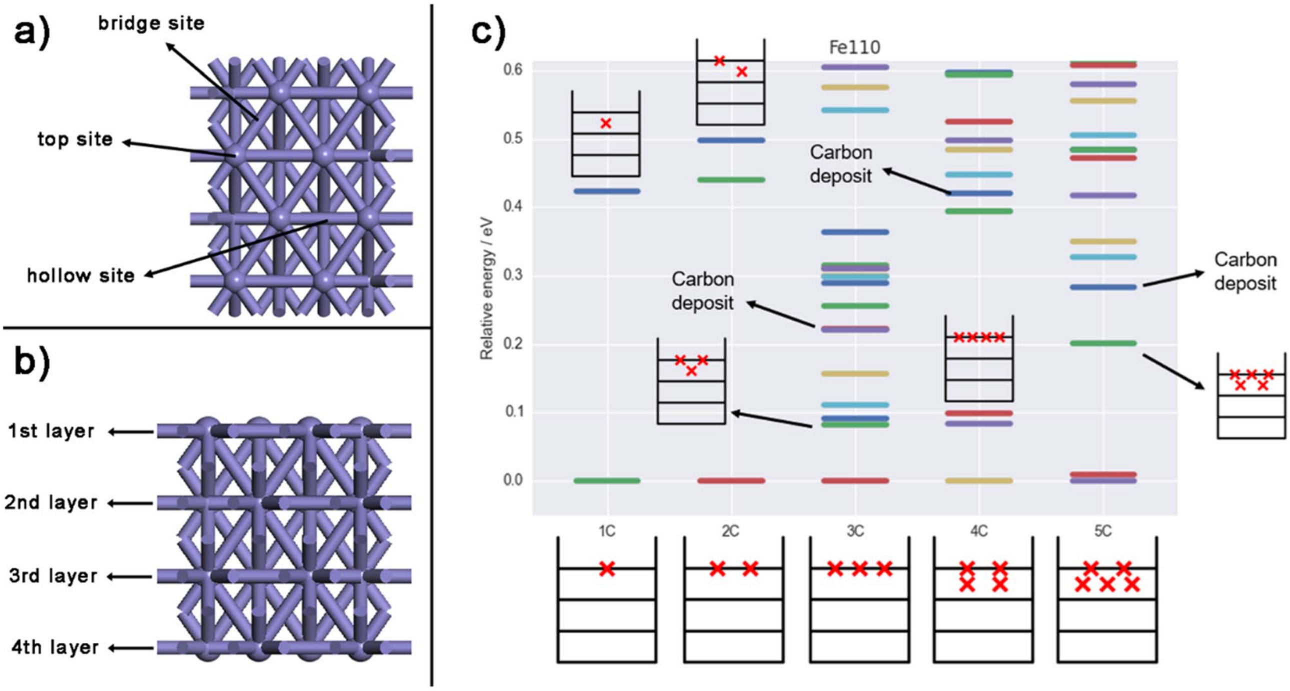

Fig. 1 (a) Top view and (b) front view of Fe(110) slab model. (c) Energy distribution and schematic illustration of carbide structures. *X* axis represents the carbon ratio from 1 to 5, and *Y* axis stands for the relative energy difference in eV, where the lowest one is set to be zero. The black horizontal lines in schemes represent iron layers, while the red crosses stand for carbon atoms.

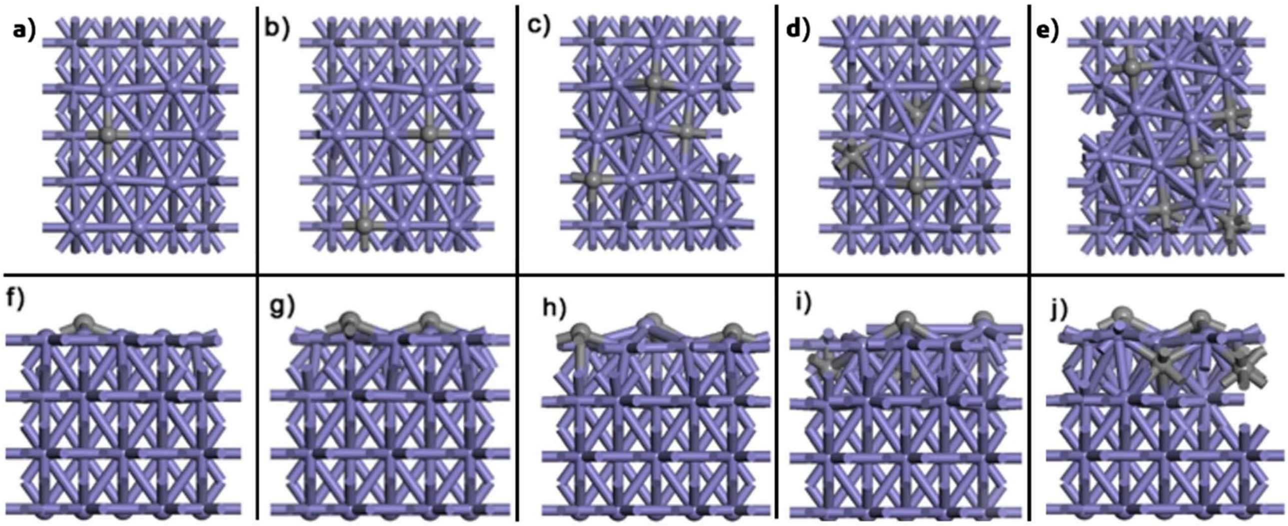

Fig. 2 (a–e) Top and (f–j) front views of the most stable Fe(110) surfaces with one to five C, respectively. Black balls represent C and purple balls stand for Fe.

the C would gradually penetrate the bulk into sub-surfaces when the number of C atoms accumulates, forming the carbide structure as observed in the experiments.[90] For carbide with one or two C, structures with low energy are quite sparse and the most stable one prevails among all. When the number of C atoms increase, however, surface structures become more flexible, and many of them are with similar stability.

Stability of carbide surfaces in the reaction conditions

The pretreatment conditions such as the ratio of reduction gases (H_2/CO), temperature, and pressure have significant effects on the stability of iron carbide surfaces.[7,9] These complicated factors can be lumped to one variable μ_C,[7] the chemical potential of carbon, which can be used to evaluate surface energy γ under experimental conditions.[7,14,24,91] Using eqn (2), the *ab initio* thermodynamics stability for carbide surfaces of Fe(100), Fe(110), and Fe(210) from 1C to 5C are plotted in Fig. 3. In this figure and following discussion, we use the total energy of a carbon atom (E_C) as the reference, *i.e.*, $\Delta\mu_C = \mu_C - E_C$. Considering the carbide formation reaction involved in synthesis gas ($CO + H_2 \rightarrow C_{(Fe)} + H_2O$), μ_C is obtained by: $\mu_C = \mu_{CO} + \mu_{H_2} - \mu_{H_2O}$, which can be expanded into:

$$\begin{aligned}\mu_c(T,P) = {} & \left[E_{CO} + \mu_{CO}(T,P^\theta) + k_B\ln\left(\frac{P_{CO}}{P^\theta}\right)\right] \\ & + \left[E_{H_2} + \mu_{H_2}(T,P^\theta) + k_B\ln\left(\frac{P_{H_2}}{P^\theta}\right)\right] \\ & - \left[E_{H_2O} + \mu_{H_2O}(T,P^\theta) + k_B\ln\left(\frac{P_{H_2O}}{P^\theta}\right)\right] \qquad (3)\end{aligned}$$

The partial pressures of the gas-phase constituents are determined by considering reaction conditions (more details in Table S9† of ref. 7). At low H_2/CO ratio (from 1 : 10 to 2.5 : 1), $\Delta\mu_C$ hardly changes and the maximum value is −7.594 eV when H_2/CO = 2.5 : 1. On the other hand, $\Delta\mu_C$ decrease significantly as the ratio continue to rise; when H_2/CO reaches 10 : 1, $\Delta\mu_C$ would be as small as −7.916 eV. The gray area in Fig. 3 represents these typical experimental $\Delta\mu_C$ range (−7.916 to −7.594), and their corresponding γ values are listed in Table 1.

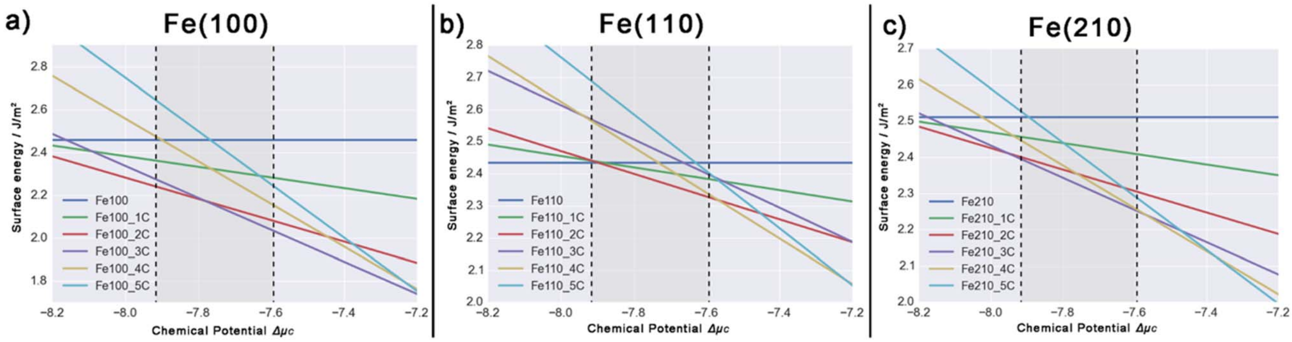

Fig. 3 *Ab initio* thermodynamics stability for carbide surfaces of Fe(100), Fe(110), and Fe(210) from 1C to 5C. *X* axis stands for the chemical potential of carbon, $\Delta\mu_C$, and *Y* axis is the surface energy in J m^{-2}. The gray area represents the typical $\Delta\mu_C$ range at experimental conditions.

Table 1 Surface energies (J m^{-2}) of Fe(100), Fe(110), and Fe(210) at the boundary of the typical experimental conditions ($\Delta\mu_C = -7.594$ and -7.916 eV). The lower the surface energy, the more stable the surface is

Surface	Fe(100)		Fe(110)		Fe(210)	
$\Delta\mu_C$ (eV)	−7.594	−7.916	−7.594	−7.916	−7.594	−7.916
Pure facet	2.46	2.46	2.44	2.44	2.51	2.51
1C	2.28	2.36	2.38	2.44	2.41	2.46
2C	2.08	2.24	2.33	2.44	2.30	2.40
3C	2.03	2.27	2.40	2.57	2.25	2.40
4C	2.15	2.47	2.34	2.56	2.26	2.45
5C	2.24	2.64	2.40	2.69	2.27	2.53

Taking Fe(100) (Fig. 3a) as an example, one can see that the surface energy of pure Fe(100) is a horizontal line, and Fe(100)-5C has the most steep slope; it is reasonable since more C on the surface means more influence by $\Delta\mu_C$; the higher the chemical potential of carbon is, the more stable the carbide with higher carbon ratio. At experimental conditions, Fe(100)-2C is the most stable one when $\Delta\mu_C < -7.78$ eV, while Fe(100)-3C become dominate after that. In Fig. 3b and c, Fe(110)-2C and Fe(210)-3C are the most stable surface, respectively. Therefore, under realistic conditions (H_2/CO ratio from 1 : 10 to 2.5 : 1 at 600 K), all three Fe surfaces are moderately carbonized (with two to three C atoms).

In addition to single facets, catalysts are more likely in a form of nanocrystals under realistic conditions. Wulff construction is a standard method to determine the equilibrium shape of bulk crystals by minimizing surface energy on given orientations. By Wulff construction, morphologies of iron crystal with Fe(100), Fe(110), and Fe(210) facets under five different $\Delta\mu_C$ are presented in Fig. 4 (detailed results are listed in Section SI-4 in the ESI†). For pure Fe ($\Delta\mu_C = -\text{Inf}$), there are about 16.9% of Fe(100), 44.5% of Fe(110), and 38.6% of Fe(210). When $\Delta\mu_C$ increase, Fe(100) expands monotonously and finally dominates the surface with a coverage of 44.6%. The percentage of Fe(110) firstly decreases to 11.4% at $\Delta\mu_C = -7.6$ eV and then starts to increase again. The percentage of Fe(210), on the contrary, increase to 56.5% until $\Delta\mu_C$ reaches −7.8 eV and then decrease to 39.8% in the end. Five crystal structures (from left to right, $\Delta\mu_C = -\text{Inf}$, −8.1, −7.8, −7.6, −7.4 eV, respectively) are illustrated in the bottom of the figure to give a visual impression of this trend.

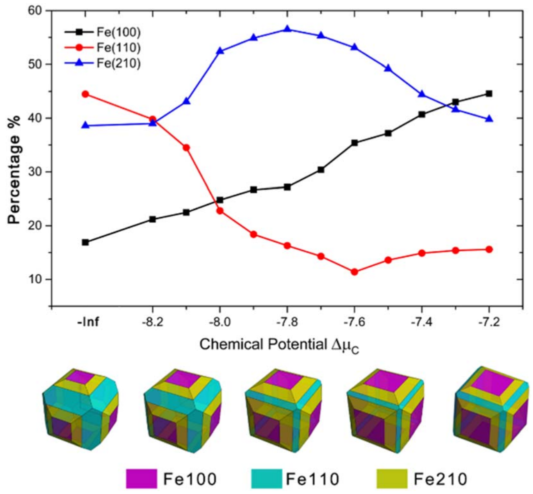

Fig. 4 Line graph of the percentage of Fe(100), Fe(110), and Fe(210) facets with respect to ΔμC. Inserts are morphologies of iron crystal with Fe(100), Fe(110), and Fe(210) facets under different $\Delta\mu_C$ by Wulffman construction (from left to right, $\Delta\mu_C = -\text{Inf}$, −8.1, −7.8, −7.6, −7.4 eV, respectively). The unit is eV and $\Delta\mu_C = -\text{Inf}$ means the chemical potential of carbon is infinitely low.

Reactivity and selectivity

In Chen *et al.*'s previous studies,[46,58–60,92] key elementary reactions of FTS were investigated, and some micro-kinetic equations, considering both energy barrier and surface coverage, were derived to quantitively evaluate the activity of FTS (details in Section SI-5 in the ESI†). To obtain the required parameters for evaluating the FTS activity, we systematically calculated the intermediates and transition states of CO dissociative adsorption, CH_x hydrogenation, and $CH_x + CH_x$ coupling process on all surfaces of Fe(100), Fe(110), and Fe(210). Regarding the H_2 dissociation, Fe is known to be a quite active metal towards H_2 dissociation, according to previous research,[93] the H_2 dissociation barrier is as low as 0.16 eV at Fe100 surface; therefore, we assume that H_2 dissociation is very fast in our study.

For the selectivity of the FTS, by considering both energy barriers and surface coverage, the following equation can be derived (details in ESI Section SI-5†):

$$r_{CH_4}/r_{C\text{–}C} \propto e^{-\Delta E_{eff}/RT} \qquad (4)$$

where r_{CH_4} and $r_{C\text{–}C}$ represent the rates of CO methanation and $C_1 + C_1$ coupling, respectively. ΔE_{eff} is the difference between the effective barrier of CH_4 formation (E_{eff,CH_4}) and chain propagation ($E_{eff,C\text{–}C}$). As we shown in ESI SI-5,† E_{eff,CH_4} is the energy difference between the transition state of CH_3–H and C + 4H in the initial state; while $E_{eff,C\text{–}C}$ is the minimum value of $E_{i,j} + E_i + E_j$. Here, E_i stands for the relative stability of CH_i with respect to a C atom, in other words, it is the energy difference between adsorbed CH_i and C + *i*H. *i* and *j* can be varied from 0 to 3, representing all possible $CH_x + CH_x$ coupling pathways on the surface. Typically, we desire a larger ΔE_{eff} value which indicates a faster $r_{C\text{–}C}$ than r_{CH_4}.

Owing to the extremely complicated reaction network of the FTS (typically more than 40 elementary reactions even in a simplified reaction model), calculating the turnover frequency of the system becomes very hard and laborious. Fortunately, it is well-known that the activity of CO hydrogenation *versus* the binding strength of C and O atoms generally shows a volcano curve,[94,95] and the rate of the FTS could be further qualitatively estimated from these descriptors.[58,96] In this study, we use the dissociative adsorption barrier of CO, $E_{C\text{–}O}$, as the indictor of the surface reactivity.[19,58]

For the reactivity and selectivity of the FTS, it should be noted that when the ratio of C to Fe is low, the C atoms are exclusively located on the surface (Fig. 2, S3, and S4†). Under steady state, surface carbon species will continuously exchange with gas phase CO flow to reach an equilibrium. Therefore, kinetically, there is no difference between clean Fe and carbides with only surface C when the coverage is low. It is the subsurface C atoms that modify their electronic and geometrical properties. This treatment is supported by the isotope labelling experiments that the exchange of ^{13}C carbon atoms in iron carbide with the reacting molecules was very slow.[97,98] According to the study of Ordomsky *et al.*[36] for FTS on $Fe^{13}C_x$ surface, ^{13}C decrease with time for all hydrocarbons, and only one ^{13}C appears on long chain products. It means that the surface C of the carbides, which were labelled by ^{13}C, involved only in the first catalytic cycle, and all following C comes from gas phase CO which then reaches an equilibrium with the surface. Therefore, in this study, we deem the reactivity and selectivity of clean surface and carbide with one and two carbons are the same.

Finally, all $E_{C\text{–}O}$ and ΔE_{eff} of Fe(100), Fe(110), Fe(210), and their carbides are calculated. Taking Fe(210)-1C and 2C for example, all structures and selective energies are show in Fig. 5 and Table 2.

As we stated in last paragraph, under steady state, the surface carbons in Fe(210)-1C and 2C would reach an equilibrium with gas phase carbon species, and there is kinetically no difference between them and pure Fe(210) surface. There is a typical B-5 site in this step surface (Fig. 5a), in which most of elementary reactions happen. Fig. 5b–e represent CO, C, and O adsorption, C and O co-adsorption, respectively. In the C–O transition state (Fig. 5f), C locates on the 3-fold hollow site on the lower terrace, while the O atom is on the 2-fold edge-bridge site, with a stretched C–O distance of 2.01 Å. The energy profile of CO dissociative adsorption is shown by the red line in Fig. 6c; we can see that the energy barrier is 0.99 eV with respect to adsorbed CO and −0.13 eV with respect to CO in the gas phase.

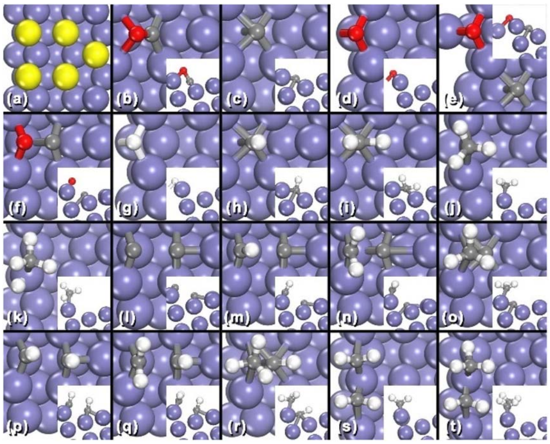

Fig. 5 Top views and side views (inserted) of the structures of (a) Fe(210) surface (B-5 site is highlighted); (b–f) CO, C, and O adsorption, C and O co-adsorption, and the transition state of CO bond breaking, respectively; (g–j) H, CH, CH_2, and CH_3 adsorption, respectively; (k–t) transition states of CH_3 + H and nine possible C_1 + C_1 coupling pathways. Black, purple, and white balls stand for C, Fe, and H, respectively.

Table 2 E_i, E_j, $E_{i,j}$, and $E_{i,j} + E_i + E_j$ of nine possible C_1 + C_1 coupling process of Fe(210)-1C. $E_{eff,C\text{–}C}$, E_{eff,CH_4}, and their energy difference ΔE_{eff} are also listed below that. All energies are thermo-corrected and the unit is eV

	$E_{i,j}$	E_i	E_j	$E_{i,j} + E_i + E_j$
C–C	3.19	0.00	0.00	3.19
C–CH	2.47	0.00	0.49	2.96
C–CH_2	1.32	0.00	1.47	2.78
C–CH_3	1.19	0.00	1.56	2.75
CH–CH	2.37	0.49	0.49	3.35
CH–CH_2	1.68	0.49	1.47	3.64
CH–CH_3	1.71	0.49	1.56	3.76
CH_2–CH_2	0.87	1.47	1.47	3.80
CH_2–CH_3	1.43	1.47	1.56	4.46
$E_{eff,C\text{–}C}$	—	—	—	2.75
E_{eff,CH_4}	—	—	—	3.01
ΔE_{eff}	—	—	—	0.25

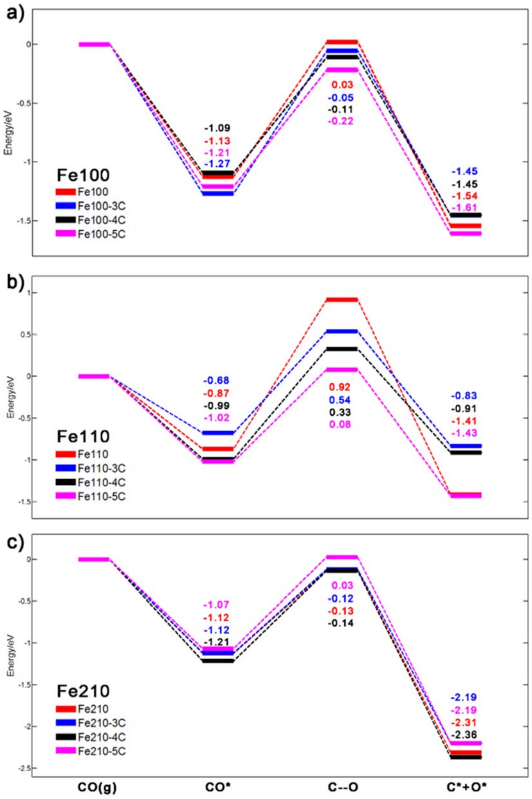

Fig. 6 Energy profiles of CO dissociative adsorption on (a) Fe(100), (b) Fe(110), and (c) Fe(210) surfaces. CO(g), CO*, C–O, and C* + O* represent CO in the gas phase, CO on the surface, the transition state, and C and O co-adsorption on the surface.

After CO dissociation, carbon species will be hydrogenated gradually. The most stable sites for CH and CH_2 are the corner sites, while the edge-bridge site is favoured by CH_3 (Fig. 5h–j). Transition states of CH_3 + H and nine possible C_1 + C_1 coupling pathways, C + C, C + CH, C + CH_2, C + CH_3, CH + CH, CH + CH_2, CH + CH_3, CH_2 + CH_2, and CH_2 + CH_3, are shown in Fig. 5k–t. With energies of these transition states, $E_{eff,C\text{–}C}$, E_{eff,CH_4}, and

Table 3 Energy barriers of CO dissociative adsorption (E_{C-O}) and ΔE_{eff} of Fe(100), Fe(110), and Fe(210). All energies are thermo-corrected and the unit is eV

	Fe(100)		Fe(110)		Fe(210)	
Surface	E_{C-O}	ΔE_{eff}	E_{C-O}	ΔE_{eff}	E_{C-O}	ΔE_{eff}
Pure facet	0.03	0.39	0.92	1.53	−0.13	0.25
1C	0.03	0.39	0.92	1.53	−0.13	0.25
2C	0.03	0.39	0.92	1.53	−0.13	0.25
3C	−0.05	0.57	0.54	1.26	−0.12	0.59
4C	−0.11	0.53	0.33	0.83	−0.14	0.55
5C	−0.22	0.76	0.08	1.01	0.03	0.03

their energy difference ΔE_{eff} are listed in Table 2. As we mentioned before, $E_{eff,C-C}$ is obtained from the minimal value of $E_{i,j} + E_i + E_j$ of all nine $C_1 + C_1$ coupling process while E_{eff,CH_4} stands for the effective barrier of CH_3 hydrogenation. For Fe(210), the difference of $E_{eff,C-C}$ and E_{eff,CH_4}, ΔE_{eff}, is 0.25 eV, indicating that $C_1 + C_1$ coupling is moderately more feasible than CH_3 hydrogenation.

Complete results of all carbide surfaces are listed in Table 3, and their energy profiles of the CO dissociative adsorption are illustrated in Fig. 6 (all relevant structures and energies are listed Section SI-6 in the ESI†). We can see that the E_{C-O} of Fe(110), a close packed surface, are very high; while the E_{C-O} of Fe(210) are the lowest among three, which is quite reasonable since the step surfaces are generally regarded more active than flat surfaces. When the number of C increases, the E_{C-O} of Fe(100) and Fe(110) decrease considerably from 0.03 to −0.22 eV and 0.92 to 0.08 eV, respectively. The E_{C-O} of Fe(210), on the other hand, remain at the same level of −0.13 eV except Fe(210)-5C. It means that the formation of iron carbide could significantly lower the energy barrier of CO dissociation adsorption of flat surfaces like Fe(100) and Fe(110), making FTS more reactive on these surfaces. For example, on pure Fe(110) surface, the FTS is nearly impossible to happen with a E_{C-O} of 0.92 eV, the incorporation of C atoms into the Fe bulk phase lower the barrier to 0.54, 0.33, and finally 0.08 eV, which makes it a probably active phase for FTS.

Fe(110) surfaces have the highest selectivity towards long chain hydrocarbons because of their large ΔE_{eff} values, although the values decrease moderately as the formation of carbide; however, that may not affect their overall activity much due to the low reactivity of Fe(110) surfaces. For both Fe(100) and Fe(210) surfaces (except Fe(210)-5C), on the other hand, ΔE_{eff} increase significantly when the carbide are formed.

Discussion

Here we are in a stage to answer the following important question: what is the origin of the high activity, as claimed in many literature,[50,53] of the iron carbide, and what is the actual active phase during FTS? There are mainly three factors that influence the activity of surfaces: stability, reactivity, and selectivity.[99] In Table 1, it is quite evident that the stability of Fe(100) and Fe(210) surfaces increase as C atoms are introduced into the system; the stability of Fe(110), on the other hand, do not vary a lot (at $\Delta\mu_C = -7.594$ eV) and even decrease when more C atoms are incorporated in (at $\Delta\mu_C = -7.916$ eV). This trend becomes more evident in Fig. 4, the surface morphologies by Wulffman construction. Starting from pure Fe particles, the surface ratio of Fe(100) and Fe(210) increase while Fe(110) shrinks significantly; Fe(210) then becomes the dominant phase in a large range of $\Delta\mu_C$ from −8.1 to 7.4 eV; it peaks around the working condition of FTS ($\Delta\mu_C$ from −7.916 to −7.594 eV). These features of surface stability show that carbides are in favour of FTS activity; as shown in last subsection, Fe(110), a close-packed surface, is quite inert while Fe(210) is active towards FTS as a step surface. Therefore, the FTS activity of Fe will benefit from the formation of carbides on the surface, because it will stabilise the FTS-active step surface rather than FTS-inert close packed surface.

In Table 3, with respect to the selectivity, both Fe(100) and Fe(210) – except Fe(210)-5C – tend to produce more long-chain hydrocarbons when the surface are carbonized, whereas for Fe(110), on the other hand, the value of ΔE_{eff} decrease, but they still remain highest among three surfaces. In Fig. 6, with respect to the reactivity, pure Fe(110) is almost inert with a high E_{C-O} of 1.79 eV (the energy difference between C–O, 0.92 eV and CO*, −0.87 eV), but the barrier drops dramatically as the C ratio increase. Therefore, for Fe(110) facet, we can safely conclude that it is the carbide that make it active towards FTS. Fe(100) has a similar trend with Fe(110); however, E_{C-O} do not vary a lot on Fe(210), which already has a relatively low E_{C-O} of ∼0.99 eV. Overall, the carbonisation of Fe surfaces will significantly lower the E_{C-O} of flat facet (Fe(100) and Fe(110)) and increase the selectivity of Fe(100) and Fe(210) towards long-chain hydrocarbons.

We can see that all three factors – stability, selectivity, and reactivity – contribute to a higher FTS activity of iron carbides. One question naturally arises here: why does this happen? Geometrically, it is obvious that the introduction of C alters the surface structure. For flat facet like Fe(100) and Fe(110) (Fig. 2 and S3†), the C atoms bend the plane and make it uneven, which provides them possible B-5-like sites to facilitate FTS process. We then analyse electronic effects of C in the system by calculating the location of the d-band center with respect to the Fermi energy, ε_d. ε_d was proposed by Nørskov and co-workers[100–102] and has been widely used to evaluate surface reactivity. For CO adsorption on surface, a higher ε_d usually means a stronger adsorption and higher reactivity. We can see from Fig. 7a that as the number of carbon atoms increase, the d-band center (ε_d) of the carbide surfaces decrease monotonously. The result indicates that the introduced C will make the surface more inert, which is opposite to the reactivity trend we have gotten before. Computational results show that geometrical effects of the C play major roles in shaping the reactivity of Fe surfaces, since the trend of d-band center (electronic effects) does not account for the strengthened CO adsorption. It is quite reasonable since Fe(210), an originally stepped surface, do not benefit from the doping of C, and E_{C-O} of Fe(210)-5C even increased, which is probably due to its electronic factors.

Finally, to combine all three factors together, we conduct a rough kinetic estimation by deeming CO dissociative

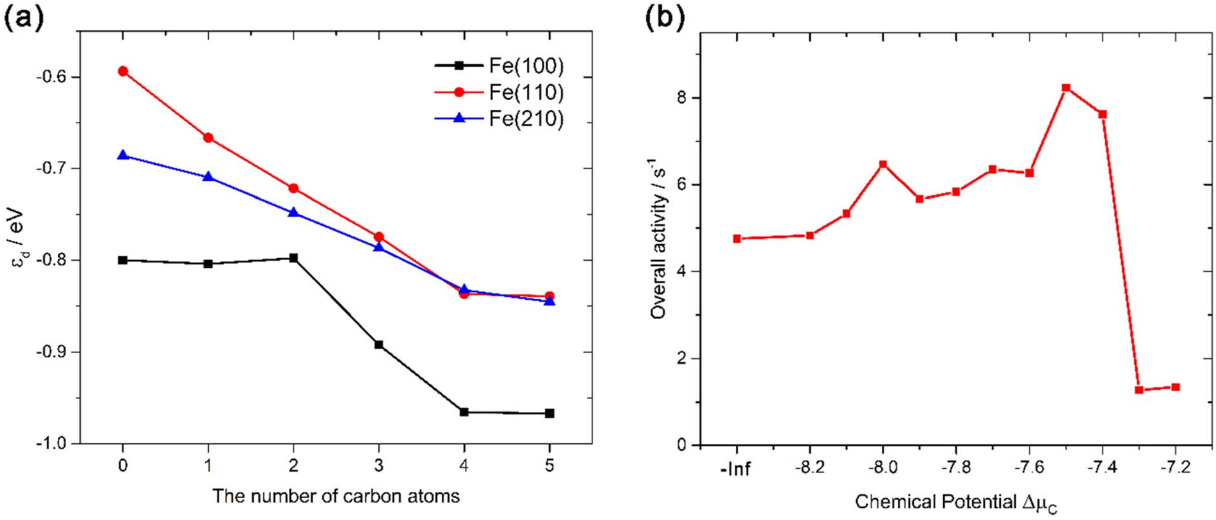

Fig. 7 Line graph of (a) d-band centers of different carbide surfaces with respect to the number of carbon atoms in the carbide; (b) the estimated overall FTS activity of the carbide surfaces *versus* chemical potential of carbon $\Delta\mu_C$. It should be noted that since the density of state (DOS) of Fe, as a magnetic material, is not symmetrical along with the *x*-axis, the spin-up d-band center ($\varepsilon_d\uparrow$) and the spin-down d-band center ($\varepsilon_d\downarrow$) are not the same;[106] ε_d used in (a) are the spin-averaged d-band center. All $\varepsilon_d\uparrow$, $\varepsilon_d\downarrow$, and ε_d values and their calculation methods are in Section SI-7 of the ESI.†

adsorption as the rate-determining step. We admit that the RDS in FTS can vary based on the catalyst used, the specific conditions under which the reaction occurs, and the particular mechanistic pathway considered. However, for many FTS catalysts, the dissociation of CO is indeed a critical step and has been proposed as the rate-determining step, especially for iron based catalysts.[103–105] For the rough estimation for general discussion, the overall rate can be expressed as:

$$r_{\text{overall}} = \sum_{\text{facet}} A P_{\text{CO}} \mathrm{e}^{-\frac{E_{\text{C-O}}}{RT}} \times \alpha \times S_{\text{facet}} \tag{5}$$

where A[107] is the pre-exponential factor and can be estimated from k_BT/h, the Boltzmann constant multiplies temperature and divided by the Planck constant. P_{CO} is the partial pressure of CO in the gas phase; α is the chain growth probability factor considered in Anderson–Schulz–Flory (ASF) kinetics model,[108] the value of which can be obtained from ΔE_{eff}:

$$\alpha = \frac{R_p}{R_p + R_t} \approx \frac{1}{1 + \mathrm{e}^{-\Delta E_{\text{eff}}/RT}} \tag{6}$$

where R_p and R_t are the rates of propagation and termination, respectively. S_{facet} is the percentage of Fe(100), Fe(110), and Fe(210) as listed in Fig. 4. We add up rates on all three facets and get r_{overall} at each chemical potential $\Delta\mu_C$, which is illustrated in Fig. 7b (detailed calculation in Section SI-7 in the ESI†). We can see that r_{overall} increase slightly as $\Delta\mu_C$ increase, but it finally plummets down when $\Delta\mu_C$ exceeds -7.3 eV. As expected, the r_{overall} increase as the carbonization of Fe surfaces. However, if we examine Fig. 7b carefully, we can notice that with a maximum rate of 8.23 s^{-1} and minimum rate of 4.75 s^{-1}; there is actually no significant difference of the rates before deactivation since their values are in the same magnitude.[109,110] As we discussed in Fig. 3, at working conditions, Fe facets are moderately carbonized with two to three C atoms on surfaces. As we shown in Fig. 6 and Table 3, at this carbonization level, the carbide does not affect the reactivity and selectivity significantly, and the rise of r_{overall} could mainly tribute to the expanded surface area of Fe(210), the active step facet. In Fig. 7b a plummet of r_{overall} is due to the increase of $E_{\text{C-O}}$ of Fe(210)-5C. Experimentally, it is also reasonable since carbons are tend to congregate on Fe(210)-5C to form coke (Fig. S2†), which could probably cause deactivation when $\Delta\mu_C$ is high.

Therefore, from above qualitative analysis, we may conclude that both Fe and iron carbide are active to FTS process. Formation of the carbide during FTS would moderately increase the reaction rate and make some originally inert facets active, but it is not essential to the overall activity of the catalysts. Rather, as we can see from the *ab initio* thermodynamics analysis, the formation of the carbide is a natural process under realistic conditions. It is also experimentally reasonable since the activation barriers of carbon diffusion into the metallic Fe structure are similar to that of the hydrogenation and polymerization at the surface.[111]

Conclusion

In summary, this work is aimed at obtaining a computational understanding of the formation of the iron carbide and their roles in catalysing Fischer–Tropsch synthesis. Given the complexities of the experimental conditions and the complexity of FTS mechanism (>100 elementary reactions), we could not claim that our simulation exactly matches experimental conditions. However, we believe our computational results could inspire experimentalists and deepen the broader understanding of FTS over Fe/FeC$_x$ surfaces.

Swarm intelligence algorithm was implemented to search most stable Fe(100), Fe(110), Fe(210) surfaces with different carbon ratios. Then, *ab initio* atomistic thermodynamics and

Wulffman construction were employed to evaluate the stability of these surfaces at different chemical potentials of carbon $\Delta\mu_C$. Their FTS reactivity and selectivity were later assessed by some micro-kinetic equations derived in our previous studies. The results and conclusions regarding carbide structures and stability are summarized in the following:

(i) The introduced C atoms tend to stay on the surface of the Fe facets; they will not penetrate into sub-surfaces to form bulk carbide until a certain concentration of C is reached.

(ii) When C concentration is low (typical with one or two C atoms), structures with low energy are quite sparse and the most stable one prevails among all. In a 2 × 2 slab model used in this study (four adsorption sites), one or two C atoms could correspond to 0.25 and 0.50C coverage.[112–114] When C coverage increase, however, surface structures become more flexible, and many of them are with similar stability.

(iii) Under realistic conditions (H_2/CO ratio from 1 : 10 to 2.5 : 1 at 600 K), all three Fe surfaces are moderately carbonized (with two to three C atoms in the model of this study, corresponding to ~0.5C coverage).

(iv) According to Wulff construction of Fe crystal, Fe(100) expands monotonously and finally dominates the surface with a coverage of 44.6%. The percentage of Fe(110) firstly decreases to 11.4% at $\Delta\mu_C = -7.6$ eV and then starts to increase again. The percentage of Fe(210), on the contrary, increase to 56.5% until $\Delta\mu_C$ reaches −7.8 eV and then decrease to 39.8% in the end. In most cases ($\Delta\mu_C$ = −8.1 to 7.4 eV), Fe(210) dominates the surface.

Regarding to FTS activity, the following conclusions are obtained:

(i) The carbonisation of Fe surfaces will significantly lower the E_{C-O} of flat facets – Fe(100) and Fe(110). Theoretically, with a reduced E_{C-O} from 1.79 to 1.10 eV, Fe(110) surface transformed from a FTS inert surface to an active one.

(ii) Using a selectivity equation derived from simplified micro-kinetic derivation, we found that the selectivity of Fe(100) and Fe(210) towards long-chain hydrocarbons are improved when the carbon ratio increases, and Fe(110) always has a highest selectivity among all three facets.

(iii) By a rough overall kinetic estimation, we suggest that both Fe and iron carbide are active to FTS process. Formation of the carbide during FTS would moderately increase the reaction rate but is not essential to the overall activity of the catalysts; it is rather a natural process under realistic conditions.

Conflicts of interest

The authors declare that they have no known competing financial interests of personal relationships that could have appeared to influence the work reported in this paper.

Acknowledgements

This research was supported by the National Natural Science Foundation of China (No. U1867221 and 52276094), the Natural Science Foundation of Hunan Province (2022JJ40038), the Changsha Science and Technology Project (kq2022141), and Joint research project of State Administration of Science, Technology and Industry for National Defense, KY20005.

References

1 R. A. van Santen, I. M. Ciobîcă, E. van Steen and M. M. Ghouri, in *Advances in Catalysis*, ed. C. G. Bruce and K. Helmut, Academic Press, 2011, vol. 54, pp. 127–187.
2 E. de Smit and B. M. Weckhuysen, *Chem. Soc. Rev.*, 2008, **37**, 2758–2781.
3 J. Cheng, P. Hu, P. Ellis, S. French, G. Kelly and C. M. Lok, *Top. Catal.*, 2010, **53**, 326–337.
4 P. Thanh Hai, Y. Qi, J. Yang, X. Duan, G. Qian, X. Zhou, D. Chen and W. Yuan, *ACS Catal.*, 2015, **5**, 2203–2208.
5 H. M. Torres Galvis, A. C. J. Koeken, J. H. Bitter, T. Davidian, M. Ruitenbeek, A. I. Dugulan and K. P. de Jong, *J. Catal.*, 2013, **303**, 22–30.
6 E. de Smit, I. Swart, J. F. Creemer, G. H. Hoveling, M. K. Gilles, T. Tyliszczak, P. J. Kooyman, H. W. Zandbergen, C. Morin, B. M. Weckhuysen and F. M. F. de Groot, *Nature*, 2008, **456**, 222–225.
7 S. Zhao, X.-W. Liu, C.-F. Huo, Y.-W. Li, J. Wang and H. Jiao, *J. Catal.*, 2012, **294**, 47–53.
8 M. Ding, Y. Yang, B. Wu, J. Xu, C. Zhang, H. Xiang and Y. Li, *J. Mol. Catal. A: Chem.*, 2009, **303**, 65–71.
9 M. Luo, H. Hamdeh and B. H. Davis, *Catal. Today*, 2009, **140**, 127–134.
10 T. Herranz, S. Rojas, F. J. Pérez-Alonso, M. Ojeda, P. Terreros and J. L. G. Fierro, *J. Catal.*, 2006, **243**, 199–211.
11 E. de Smit, A. M. Beale, S. Nikitenko and B. M. Weckhuysen, *J. Catal.*, 2009, **262**, 244–256.
12 M. A. Petersen, J.-A. van den Berg and W. J. van Rensburg, *J. Phys. Chem. C*, 2010, **114**, 7863–7879.
13 J. M. Gracia, F. F. Prinsloo and J. W. Niemantsverdriet, *Catal. Lett.*, 2009, **133**, 257–261.
14 E. de Smit, F. Cinquini, A. M. Beale, O. V. Safonova, W. van Beek, P. Sautet and B. M. Weckhuysen, *J. Am. Chem. Soc.*, 2010, **132**, 14928–14941.
15 T. Riedel, H. Schulz, G. Schaub, K.-W. Jun, J.-S. Hwang and K.-W. Lee, *Top. Catal.*, 2003, **26**, 41–54.
16 M. D. Shroff, D. S. Kalakkad, K. E. Coulter, S. D. Kohler, M. S. Harrington, N. B. Jackson, A. G. Sault and A. K. Datye, *J. Catal.*, 1995, **156**, 185–207.
17 S. Li, W. Ding, G. D. Meitzner and E. Iglesia, *J. Phys. Chem. B*, 2002, **106**, 85–91.
18 S. Li, G. D. Meitzner and E. Iglesia, *J. Phys. Chem. B*, 2001, **105**, 5743–5750.
19 J. X. Liu and W. X. Li, *Wiley Interdiscip. Rev. Comput. Mol. Sci.*, 2016, **6**, 571–583.
20 S. Zhao, X.-W. Liu, C.-F. Huo, X.-D. Wen, W. Guo, D. Cao, Y. Yang, Y.-W. Li, J. Wang and H. Jiao, *Catal. Today*, 2015, 93–100, DOI: **10.1016/j.cattod.2015.07.035**.
21 M. O. Ozbek and J. W. Niemantsverdriet, *J. Catal.*, 2014, **317**, 158–166.
22 P. Thanh Hai, X. Duan, G. Qian, X. Zhou and D. Chen, *J. Phys. Chem. C*, 2014, **118**, 10170–10176.

23 R. Gao, D.-B. Cao, S. Liu, Y. Yang, Y.-W. Li, J. Wang and H. Jiao, *Appl. Catal., A*, 2013, **468**, 370–383.
24 S. Zhao, X.-W. Liu, C.-F. Huo, Y.-W. Li, J. Wang and H. Jiao, *Catal., Struct. React.*, 2015, **1**, 44–60.
25 B. Wang, X. Yu, C. Huo, J. Wang and Y. Li, *Chin. J. Catal.*, 2014, **35**, 28–37.
26 K. Xu, B. Sun, J. Lin, W. Wen, Y. Pei, S. Yan, M. Qiao, X. Zhang and B. Zong, *Nat. Commun.*, 2014, **5**, 5783.
27 X.-Y. Liao, D.-B. Cao, S.-G. Wang, Z.-Y. Ma, Y.-W. Li, J. Wang and H. Jiao, *J. Mol. Catal. A: Chem.*, 2007, **269**, 169–178.
28 H. Zhao, J.-X. Liu, C. Yang, S. Yao, H.-Y. Su, Z. Gao, M. Dong, J. Wang, A. I. Rykov, J. Wang, Y. Hou, W.-X. Li and D. Ma, *CCS Chem.*, 2021, **3**, 2712–2724.
29 J. Cheng, P. Hu, P. Ellis, S. French, G. Kelly and C. M. Lok, *J. Phys. Chem. C*, 2010, **114**, 1085–1093.
30 R. Gao, X. Liu, Z. Cao, X. Liu, K. Louis, D. Ma, Y. Yang, Y.-W. Li, R. Hoffmann and X.-D. Wen, *Catal. Lett.*, 2019, **149**, 1–20.
31 C. S. Kuivila, P. C. Stair and J. B. Butt, *J. Catal.*, 1989, **118**, 299–311.
32 J. B. Butt, *Catal. Lett.*, 1990, **7**, 61–81.
33 D. Mahajan, P. Gütlich, J. Ensling, K. Pandya, U. Stumm and P. Vijayaraghavan, *Energy Fuels*, 2003, **17**, 1210–1221.
34 J. W. Niemantsverdriet, A. M. Van der Kraan, W. L. Van Dijk and H. S. Van der Baan, *J. Phys. Chem.*, 1980, **84**, 3363–3370.
35 C.-K. Kuei and M.-D. Lee, *J. Mol. Catal.*, 1991, **65**, 293–305.
36 V. V. Ordomsky, B. Legras, K. Cheng, S. Paul and A. Y. Khodakov, *Catal. Sci. Technol.*, 2015, **5**, 1433–1437.
37 D. B. Bukur, L. Nowicki, R. K. Manne and X. S. Lang, *J. Catal.*, 1995, **155**, 366–375.
38 N. Sirimanothan, H. H. Hamdeh, Y. Zhang and B. H. Davis, *Catal. Lett.*, 2002, **82**, 181–191.
39 R. A. van Santen, A. J. Markvoort, I. A. Filot, M. M. Ghouri and E. J. Hensen, *Phys. Chem. Chem. Phys.*, 2013, **15**, 17038–17063.
40 F. Fischer and H. Tropsch, *Brennst. Chem.*, 1926, **7**, 97–104.
41 J. T. Kummer and P. H. Emmett, *J. Am. Chem. Soc.*, 1953, **75**, 5177–5183.
42 H. Pichler and H. Schultz, *Chem. Ing. Tech.*, 1970, **12**, 1160–1174.
43 Z. Teimouri, N. Abatzoglou and A. K. Dalai, *Catalysts*, 2021, **11**, 330.
44 L. Zhou, J. Gao, X. Hao, Y. Yang and Y. Li, *Reactions*, 2021, **2**, 161–174.
45 M. Martinelli, M. K. Gnanamani, S. LeViness, G. Jacobs and W. D. Shafer, *Appl. Catal., A*, 2020, **608**, 117740.
46 J. Cheng, X. Q. Gong, P. Hu, C. M. Lok, P. Ellis and S. French, *J. Catal.*, 2008, **254**, 285–295.
47 Z. P. Liu and P. Hu, *J. Am. Chem. Soc.*, 2002, **124**, 11568–11569.
48 R. C. Brady and R. Pettit, *J. Am. Chem. Soc.*, 1981, **103**, 1287–1289.
49 R. A. van Santen, A. J. Markvoort, M. M. Ghouri, P. A. J. Hilbers and E. J. M. Hensen, *J. Phys. Chem. C*, 2013, **117**, 4488–4504.
50 B. Chen, D. Wang, X. Duan, W. Liu, Y. Li, G. Qian, W. Yuan, A. Holmen, X. Zhou and D. Chen, *ACS Catal.*, 2018, **8**, 2709–2714.
51 T. H. Pham, Y. Qi, J. Yang, X. Duan, G. Qian, X. Zhou, D. Chen and W. Yuan, *ACS Catal.*, 2015, **5**, 2203–2208.
52 J. Ren, N. Ai and Y. Yu, *RSC Adv.*, 2021, **11**, 34533–34543.
53 Y. Chen, L. Ma, R. Zhang, R. Ye, W. Liu, J. Wei, V. V. Ordomsky and J. Liu, *Appl. Catal., B*, 2022, **312**, 121393.
54 A. Chakraborty and A. Kar, *Nature-Inspired Computing and Optimization*, 2017, pp. 475–494, DOI: 10.1007/978-3-319-50920-4_19.
55 A. Rajan, A. P. Pushkar, B. C. Dharmalingam and J. J. Varghese, *iScience*, 2023, **26**, 107029.
56 J. Cao, N. Song, W. Chen, Y. Cao, G. Qian, X. Duan and X. Zhou, *Chem.–Asian J.*, 2020, **15**, 4014–4022.
57 X. Wang, N. Liu, Q. Zhang, X. Liang, B. Chen and D. Mei, *Particuology*, 2020, **48**, 2–12.
58 J. Cheng, P. Hu, P. Ellis, S. French, G. Kelly and C. M. Lok, *J. Phys. Chem. C*, 2010, **114**, 1085–1093.
59 J. Cheng, P. Hu, P. Ellis, S. French, G. Kelly and C. M. Lok, *J. Phys. Chem. C*, 2009, **113**, 8858–8863.
60 J. Cheng, P. Hu, P. Ellis, S. French, G. Kelly and C. M. Lok, *J. Phys. Chem. C*, 2008, **112**, 6082–6086.
61 J. P. Perdew, K. Burke and M. Ernzerhof, *Phys. Rev. Lett.*, 1996, **77**, 3865–3868.
62 G. Kresse and J. Furthmüller, *Comput. Mater. Sci.*, 1996, **6**, 15–50.
63 G. Kresse and J. Hafner, *Phys. Rev. B: Condens. Matter Mater. Phys.*, 1994, **49**, 14251–14269.
64 G. Kresse and D. Joubert, *Phys. Rev. B: Condens. Matter Mater. Phys.*, 1999, **59**, 1758–1775.
65 P. E. Blöchl, O. Jepsen and O. K. Andersen, *Phys. Rev. B: Condens. Matter Mater. Phys.*, 1994, **49**, 16223–16233.
66 B. Liu, W. Li, J. Zheng, Q. Lin, X. Zhang, J. Zhang, F. Jiang, Y. Xu and X. Liu, *Catal. Sci. Technol.*, 2018, **8**, 5288–5301.
67 A. Stibor, G. Kresse, A. Eichler and J. Hafner, *Surf. Sci.*, 2002, **507–510**, 99–102.
68 Z. Yao, C. Guo, Y. Mao and P. Hu, *ACS Catal.*, 2019, **9**, 5957–5973.
69 J.-F. Chen, Y. Mao, H.-F. Wang and P. Hu, *ACS Catal.*, 2019, **9**, 2633–2638.
70 Y. Liu, H. Liu, L. Luo, B. Lin, Y. Zhou, H. Wang, P. Wang and Y. Mao, *ChemCatChem*, 2023, **15**, e202201544.
71 Y. Mao, Z. Wang, H.-F. Wang and P. Hu, *ACS Catal.*, 2016, 7882–7891, DOI: 10.1021/acscatal.6b01449.
72 Z. Wang, X. M. Cao, J. Zhu and P. Hu, *J. Catal.*, 2014, **311**, 469–480.
73 A. Alavi, P. Hu, T. Deutsch, P. L. Silvestrelli and J. Hutter, *Phys. Rev. Lett.*, 1998, **80**, 3650–3653.
74 Z.-P. Liu and P. Hu, *J. Am. Chem. Soc.*, 2003, **125**, 1958–1967.
75 Y. Wang, J. Lv, L. Zhu and Y. Ma, *Comput. Phys. Commun.*, 2012, **183**, 2063–2070.
76 Y. Wang, J. Lv, L. Zhu and Y. Ma, *Phys. Rev. B: Condens. Matter Mater. Phys.*, 2010, **82**, 094116.
77 Y. Wang, F. Li, Y. Li and Z. Chen, *Nat. Commun.*, 2016, **7**, 11488.

78 S. Lu, Y. Wang, H. Liu, M. S. Miao and Y. Ma, *Nat. Commun.*, 2014, **5**, 3666.

79 X. Tian, S. Wang, Z.-j. Wang, H. Wang, Y. Zhou, H. Zhong and Y. Mao, *ChemCatChem*, 2020, **12**, 3240–3248.

80 S. Lu, Y. Wang, H. Liu, M.-s. Miao and Y. Ma, *Nat. Commun.*, 2014, **5**, 3666.

81 Y. Wang, J. Lv, P. Gao and Y. Ma, *Acc. Chem. Res.*, 2022, **55**, 2068–2076.

82 K. Reuter and M. Scheffler, *Phys. Rev. B: Condens. Matter Mater. Phys.*, 2003, **68**, 045407.

83 K. Reuter and M. Scheffler, *Phys. Rev. B: Condens. Matter Mater. Phys.*, 2001, **65**, 035406.

84 Y. Mao and P. Hu, *Sci. China Chem.*, 2020, **63**, 850–859.

85 R. V. Zucker, D. Chatain, U. Dahmen, S. Hagège and W. C. Carter, *J. Mater. Sci.*, 2012, **47**, 8290–8302.

86 A. R. Roosen, R. P. McCormack and W. C. Carter, *Comput. Mater. Sci.*, 1998, **11**, 16–26.

87 G. D. Barmparis, Z. Lodziana, N. Lopez and I. N. Remediakis, *Beilstein J. Nanotechnol.*, 2015, **6**, 361–368.

88 S. Li, R. J. O'Brien, G. D. Meitzner, H. Hamdeh, B. H. Davis and E. Iglesia, *Appl. Catal., A*, 2001, **219**, 215–222.

89 M. E. Dry, T. Shingles, L. J. Boshoff and C. S. van H. Botha, *J. Catal.*, 1970, **17**, 347–354.

90 X. Liu, J. Liu, Y. Yang, Y.-W. Li and X. Wen, *ACS Catal.*, 2021, **11**, 2156–2181.

91 E. de Smit, M. M. van Schooneveld, F. Cinquini, H. Bluhm, P. Sautet, F. M. de Groot and B. M. Weckhuysen, *Angew. Chem., Int. Ed.*, 2011, **50**, 1584–1588.

92 J. Cheng, T. Song, P. Hu, C. M. Lok, P. Ellis and S. French, *J. Catal.*, 2008, **255**, 20–28.

93 E. van Steen and P. van Helden, *J. Phys. Chem. C*, 2010, **114**, 5932–5940.

94 J. Cheng, P. Hu, P. Ellis, S. French, G. Kelly and C. M. Lok, *J. Phys. Chem. C*, 2008, **112**, 1308–1311.

95 T. Bligaard, J. K. Nørskov, S. Dahl, J. Matthiesen, C. H. Christensen and J. Sehested, *J. Catal.*, 2004, **224**, 206–217.

96 I. A. Filot, R. A. van Santen and E. J. Hensen, *Angew. Chem., Int. Ed.*, 2014, **53**, 12746–12750.

97 D. M. Stockwell, D. Bianchi and C. O. Bennett, *J. Catal.*, 1988, **113**, 13–24.

98 H. Matsumoto and C. O. Bennett, *J. Catal.*, 1978, **53**, 331–344.

99 G. P. Van Der Laan and A. A. C. M. Beenackers, *Catal. Rev.*, 1999, **41**, 255–318.

100 B. Hammer and J. K. Norskov, *Nature*, 1995, **376**, 238–240.

101 J. K. Nørskov, F. Studt, F. Abild-Pedersen and T. Bligaard, *Fundamental Concepts in Heterogeneous Catalysis*, John Wiley & Sons, Inc., Hoboken, New Jersey, 2014.

102 C.-F. Huo, Y.-W. Li, J. Wang and H. Jiao, *J. Am. Chem. Soc.*, 2009, **131**, 14713–14721.

103 Sonal, K. Kondamudi, K. K. Pant and S. Upadhyayula, *Ind. Eng. Chem. Res.*, 2017, **56**, 4659–4671.

104 J. Yang, Y. Qi, J. Zhu, Y.-A. Zhu, D. Chen and A. Holmen, *J. Catal.*, 2013, **308**, 37–49.

105 G. R. Johnson, S. Werner and A. T. Bell, *ACS Catal.*, 2015, **5**, 5888–5903.

106 S. Bhattacharjee, U. V. Waghmare and S. C. Lee, *Sci. Rep.*, 2016, **6**, 35916.

107 J. K. Nørskov, F. Studt, F. Abild-Pedersen and T. Bligaard, in *Fundamental Concepts in Heterogeneous Catalysis*, 2014, pp. 47–67.

108 R. B. Anderson, *Catalysts for the Fischer–Tropsch Synthesis*, Van Nostrand Reinhold, New York, 1956.

109 K. Honkala, A. Hellman, I. N. Remediakis, A. Logadottir, A. Carlsson, S. Dahl, C. H. Christensen and J. K. Nørskov, *Science*, 2005, **307**, 555–558.

110 T. Wang, X.-X. Tian, Y.-W. Li, J. Wang, M. Beller and H. Jiao, *ACS Catal.*, 2014, **4**, 1991–2005.

111 J. W. Niemantsverdriet and A. M. van der Kraan, *J. Catal.*, 1981, **72**, 385–388.

112 T. Li, X. Wen, Y.-W. Li and H. Jiao, *J. Phys. Chem. C*, 2019, **123**, 25657–25667.

113 I. V. Mutigullin, D. I. Bazhanov and A. S. Ilyushin, *Phys. Solid State*, 2011, **53**, 599–605.

114 C. Guo, Y. Mao, Z. Yao, J. Chen and P. Hu, *J. Catal.*, 2019, **379**, 52–59.